A nonlinear beam model of photomotile structures

Kevin Korner, Alexa S Kuenstler, Ryan C Hayward, Basile Audoly, Kaushik Bhattacharya

A nonlinear beam model of photomotile structures

Kevin Korner[1], Alexa Kuenstler[2], Ryan Hayward[2], Basile Audoly[3], and Kaushik Bhattacharya[1]

[1]Division of Engineering and Applied Science, California Institute of Technology, USA
[3]Laboratoire de mécanique des solides, CNRS, Institut Polytechnique de Paris, Palaiseau, France
[2]Department of Polymer Science and Engineering, University of Massachusetts, Amherst, USA

November 16, 2020

Actuation remains a significant challenge in soft robotics. Actuation by light has important advantages: objects can be actuated from a distance, distinct frequencies can be used to actuate and control distinct modes with minimal interference and significant power can be transmitted over long distances through corrosion-free, lightweight fiber optic cables. Photochemical processes that directly convert photons to configurational changes are particularly attractive for actuation. Various works have reported light-induced actuation with liquid crystal elastomers combined with azobenzene photochromes. We present a simple modeling framework and a series of examples that studies actuation by light. Of particular interest is the generation of cyclic or periodic motion under steady illumination. We show that this emerges as a result of a coupling between light absorption and deformation. As the structure absorbs light and deforms, the conditions of illumination change, and this in turn changes the nature of further deformation. This coupling can be exploited in either closed structures or with structural instabilities to generate cyclic motion.

Keywords *Actuation, Photomechanical materials, Liquid crystal elastomers, Azobenzene, Propulsion.*

Significance *Actuation and propulsion are significant challenges in soft robotics. Supply of power typically requires a cumbersome tether or heavy on-board power source. Further, one typically needs to reset the system. Using theory and numerical simulations, we show in this work that this challenge can be overcome by the use of photo-mechanical materials and actuation by light. We develop a simple modeling framework which reveals how steady illumination from a distance can give rise to cyclic motion. Such motion can be exploited for actuation and propulsion with no need for tether or on-board power source, through the natural but nonlinear/non-local coupling between deformation and light absorption.*

A major challenge in soft robotics is the integration of sensing, actuation, control, and propulsion. In most soft robotic systems, propulsion and controls are enabled through a physical tether or complex on-board electronics and batteries. A tether simplifies the design but limits the range of motion of the robot, while on-board controls and power supplies can be heavy and can complicate the design [1]. Actuation by light through photomechanical processes directly converts photons to deformation and offers an attractive alternative. It can deliver energy remotely. Further, multiple frequencies can be used to actuate and sense different modes. Finally, if a tether is an option, then a significant energy can be delivered through corrosion-free and lightweight fiber-optic cables.

A further challenge arises in propulsion where one needs to generate cyclic motion. Since most actuation systems actuate one way, there is a need to reset the system [1]. To simplify the control process, it is desirable to do so by inherent response rather than by pulsing of the external source. Actuation by light is again attractive because one can use the directionality of the propagation of light. As the structure absorbs light and deforms, the conditions of illumination change, and this in turn changes the nature of further deformation. This coupling can be exploited in either closed structures or with structural instabilities to generate cyclic motion.

These advantages have motivated a recent body of work on developing photomechanical materials (see [9] for an extensive review). Much of this work has focussed on incorporating azobenzene photochromes that absorb light and transform between *cis* and *trans* configurations into liquid crystal elastomers whose orientational order is coupled to deformation, following the pioneering work of Yu *et al.* [13]. These materials are typically synthesized as thin strips which bend when illuminated with light of appropriate frequency. Further they can be combined with structural polymers to provide robustness [4].

Various works have demonstrated the ability to generate cyclic motion under steady illumination. Yamada *et al.* [12] demonstrated that a ring of liquid crystal elastomer (LCE) film containing azobenzene derivatives can roll in the presence of illumination. When wrapped around a series of pulleys, the film can be used as a light-driven plastic motor system. White *et al.* [10] developed a high frequency oscillator from a strip which bends under illumination sufficiently to block the light source and reset. Wei *et al.* [11] produced rolling motion in monolithic polymer films where ultraviolet-visible light transforms the film from flat sheets to spiral ribbons, which then rolls under continuous illumination. Finally, Gelebart *et al.* [4] created an oscillatory behavior of a doubly clamped LCE film.

Modeling light-mediated actuation is a complex multiphysics process involving three key elements: propagation and absorption of light, chemical transformation and temporal evolution of chromophores between states, and the nonlinear mechanics of structures undergoing large deformations. Corbett and Warner analyzed light absorption and actuation in azobenzene containing liquid crystal elastomers [2] and proposed a geometrical theory of illuminated thin strips [3]; this theory assumes that the stress in the strip remains zero, and is only applicable to the special case when the strips are unconstrained. While this model reveals various aspects of photo-actuation, it is unable to explain the cyclic behavior in the experiments above, where the constraints applied on the ends of strips, either through boundary conditions [4] or as a closed loop [12], give rise to internal stress.

In this paper, we build on the work of Corbett and Warner [3] by coupling it to the mechanics of beams, and derive a fully coupled photo-activated mechanical model for thin illuminated strips which can handle arbitrary boundary conditions. Remarkably, a number of material, physical parameters – time-constants of photo-activation and relaxation, penetration depth, the elastic

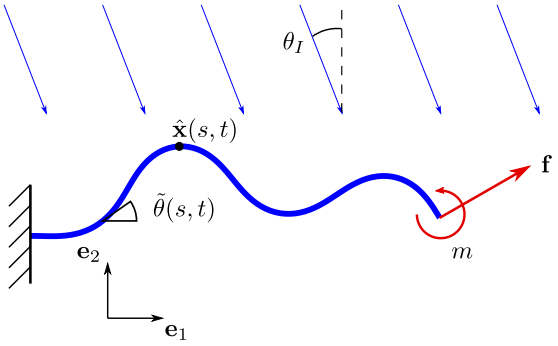

Figure 1: Elastica under illumination.

modulus and thickness of the strip and illumination intensity – collapse into a single non-dimensional parameter that governs the behavior. This highlights the flexibility that is available in the choice of material and structure in the development of light-activated structures. Our resulting model is simple and can be solved numerically in real time on any personal computer, while capturing a rich range of behaviors. We use it to address cyclic or periodic motion under steady illumination and reveal the underlying mechanisms. The ability of this simple model to capture complex dynamics of light illuminated deformation make it a useful tool for the design and control of this novel type of structures.

1 Photo-deformable elastica

Consider an inextensible beam or a strip (planar elastica) subjected to illumination as shown in Figure 1. Let $\mathbf{x}(s,t)$ denote the position of centerline point s at time t and $\theta(s,t)$ denote the angle that the tangent to the beam makes with the horizontal axis $\mathbf{e}_1$. We assume that the deformation caused by illumination takes place over a significantly slower time scale than the natural periods of vibration of the beam so that we may assume that the beam is at equilibrium at all times. Therefore, at each t,

$$\frac{\partial \mathbf{f}}{\partial s}(s,t) = 0, \tag{1}$$

$$\frac{\partial m}{\partial s}(s,t) + (\widehat{\mathbf{t}}(s,t) \times \mathbf{f}(s,t)) \cdot \mathbf{e}_3 = 0 \tag{2}$$

where $\widehat{\mathbf{t}}(\theta(s,t)) = \partial \mathbf{x}/\partial s(s,t) = \cos\theta(s,t)\mathbf{e}_1 + \sin\theta(s,t)\mathbf{e}_2$ is the unit tangent, $\mathbf{f}(s,t)$ is the internal force transmitted across a cross-section, and $m(s,t)$ is the internal moment about $\mathbf{e}_3$.

Since we assume that the beam is inextensible and unshearable, the internal force $\mathbf{f}$ is constitutively indeterminate and we only need to specify a constitutive law for the moment m. Following Corbett and Warner [3], we assume that the beam is made of an elastic material whose spontaneous or stress-free strain, ε_0, changes with time depending on the local population of *cis* molecules. The longitudinal stress at a point at a position s along the length of the beam, z along the depth of the beam and at time t is given by Hooke's law, $\sigma(s,z,t) = E(\varepsilon(s,z,t) - \varepsilon_0(s,z,t))$, where ε is the strain and ε_0 is the spontaneous strain. The moment is found by integration through the thickness

as

$$m(s,t) = \int_{-h/2}^{h/2} E(\varepsilon(s,z,t) - \varepsilon_0(s,z,t))z\mathrm{d}z \tag{3}$$

where h is the thickness of the beam and $z = 0$ is taken to be the center of the beam. The strain is related to curvature as in classical elastica theory[1], and the spontaneous strain depends on the built-in curvature κ_r of the beam (the curvature with no applied load and no illumination) and the concentration n_c of the *cis* molecules:

$$\varepsilon(s,z,t) = \kappa(s,t)z, \tag{4}$$

$$\varepsilon_0(s,z,t) = \kappa_r(s)z - \lambda n_c(s,z,t) \tag{5}$$

where λ is a constant of proportionality linking the longitudinal strain and concentration of *cis* molecules. $\lambda > 0$ is when the *cis* molecules corresponds to an expansion, while $\lambda < 0$ corresponds to an induced contraction. This depends on the orientation of the director of the LCE. If the strip is made with directors parallel to the the length of the strip (as in the 'planar' face of Gelebart *et al.*), illumination produces a contraction along the length and therefore $\lambda < 0$. If, on the other hand, the strip is made with the director along the normal to the strip (as in the 'homoetropic' face of Gelebart *et al.*), illumination causes an elongation along the length of the strip and therefore $\lambda > 0$.

Substituting (4) and (5) into (3), we find the constitutive law in the form

$$m(s,t) = \frac{Eh^3}{12}(\kappa(s,t) - \kappa_0(s,t)) \tag{6}$$

where

$$\kappa_0(s,t) = \kappa_r(s) - \frac{12\lambda}{h^3}\int_{-h/2}^{h/2} n_c(s,z,t)z\mathrm{d}z. \tag{7}$$

It remains to specify the evolution of the spontaneous curvature in the presence of illumination. The concentration of *cis* molecules is increased by photon absorption, and decreased by thermal decay [3]:

$$\frac{\partial n_c}{\partial t}(s,z,t) = -\kappa_1 n_c(s,z,t) + (1 - n_c(s,z,t))\kappa_2\tilde{\alpha}_1\mathcal{I}(s,z,t),$$

where n_c is the fraction of activated chromophores, $\tilde{\alpha}_1$ is a material constant which measures the efficiency of the production of *cis* isomers by incident light, and $\mathcal{I}(s,z,t)$ denotes the illumination, *i.e.*, the quantity of photons per unit time arriving at the depth z at time t. κ_1 and κ_2 are the thermal decay and the forward isomerization reaction rates, respectively. In typical materials, $n_c \ll 1$ is small [9] so we can simplify the differential equation to

$$\tau\frac{\partial n_c}{\partial t}(s,z,t) = n_c(s,z,t) + \alpha_1\mathcal{I}(s,z,t)\,, \tag{8}$$

where $\tau = 1/\kappa_1$ and $\alpha_1 = \kappa_2\tilde{\alpha}_1/\kappa_1$. Further, at any location s along the length of the strip, the intensity diminishes with depth with the number of photons absorbed [3]

$$\frac{\partial \mathcal{I}}{\partial z} = -\frac{1 - n_c}{d}\mathcal{I}(s,z,t)$$

[1]We assume that the neutral axis is unaffected by illumination since the penetration depth is small, as argued later.

where d is the penetration depth. So, when $n_c \ll 1$, the intensity follows Beer's law

$$\mathcal{I}(s,z,t) = \mathcal{I}_0(s,t)\exp\left(-\frac{h/2-z}{d}\right) \tag{9}$$

where $z = h/2$ is the free surface that is illuminated and $\mathcal{I}_0$ is the intensity of light on the illuminated surface[2]. Combining (7), (8) and (9),

$$\tau\frac{\partial\kappa_0}{\partial t}(s,t) = -\frac{12\lambda}{h^3}\int_{-h/2}^{h/2}\tau\frac{\partial n_c}{\partial t}(s,z,t)z\mathrm{d}z = -(\kappa_0(s,t)-\kappa_r(s)) + \alpha\mathcal{I}_0(s,t)$$

where $\alpha = -\frac{12\lambda\alpha_1}{h^3}\int_{-h/2}^{h/2}\exp\left(-\frac{h/2-z}{d}\right)z\mathrm{d}z$ is an effective (macroscopic) coupling constant. Finally, the absorption of light on the surface depends on light intensity I_0 and on the relative orientation of the light and the strip, $\mathcal{I}_0(s,t) = I_0 f(\theta(s,t)-\theta_I)$, where θ_I is the angle of illumination. Therefore,

$$\tau\frac{\partial\kappa_0}{\partial t}(s,t) + (\kappa_0(s,t)-\kappa_r(s)) = \alpha I_0 f(\theta(s,t)-\theta_I). \tag{10}$$

The projection function f is chosen as

$$f(\phi) = \begin{cases} \cos\phi & \text{if } \phi \in (-\pi/2,\pi/2), \\ 0 & \text{else.} \end{cases} \tag{11}$$

This f accounts for self-shadowing in an approximate but effective way: in our examples, the parts of the rods that are exposed to the light source are such that $\phi \in (-\pi/2,\pi/2)$ and in that case the coefficient $\cos\phi$ accounts for the reduction in light flux per unit area due to the non-normal incidence. Regions such that $\phi \notin (-\pi/2,\pi/2)$ are considered to be shadowed by other parts of the rod.

Finally, we combine (1), (2), (4) and (6), and non-dimensionalize the resulting equation along with (10), introducing the scaled arclength $S = s/l$ (where l is the length of the beam), the scaled time $T = t/\tau$ and the scaled curvature $K = l\kappa$,

$$\frac{\partial}{\partial S}\left(\frac{\partial\theta}{\partial S}(S,T) - K_0(S,T)\right) - F_x\cos\theta(S,T) + F_y\sin\theta(S,T) = 0, \tag{12}$$

$$\frac{\partial K_0}{\partial T}(S,T) + (K_0(S,T)-K_r(S)) = \Lambda f(\theta(S,T)-\theta_I). \tag{13}$$

The constants F_x and F_y are Lagrange multipliers that enforce the inextensibility. Remarkably, these equations depend on two parameters only: the angle of illumination θ_I and the dimensionless constant

$$\Lambda = \alpha l I_0 = -\frac{12\kappa_2\tilde{\alpha}_1\mathcal{I}_0}{\kappa_1 h^3}\int_{-h/2}^{h/2}\exp\left(-\frac{h/2-z}{d}\right)z\mathrm{d}z \tag{14}$$

that encompasses various material and physical parameters—time constants of photo-activation and relaxation, penetration depth, the elastic modulus and thickness of the strip and illumination intensity. The fact that so many material and physical parameters collapse into a single

[2]Note that the result (10) does not require the exponential profile of Beer's law, but simply a steady profile, $\mathcal{I}(s,z,t) = \mathcal{I}_0(s,t)f(z)$. Also note that the failure of the condition $n_c \ll 1$ leads to bleaching and other effects discussed in [3] and [5].

Parameter	Typical Value
$\lambda\alpha_1$	$-5.4 * 10^{-5}$ $\mathrm{m^2W^{-1}}$ [8]
I_0	100 $\mathrm{W/m^2}$ [8]
E	$0.6 - 4$ GPa [8]
h	15 μm [8]
d	0.56 μm [6]
w	1 mm [8]
l	15 mm [8]

Table 1: Estimates of the experimental parameters based on the literature.

non-dimensional parameter highlights the flexibility that is available in the choice of material and structure in the development of light-activated structures. Since the dimensionless equations are governed by a single dimensionless parameter Λ, we are able to characterize all the possible behaviors in a given geometry simply by sweeping over Λ. Based on the values in Table 1 estimated from literature reports on a glassy azobenzene-functionalized polyimide, we obtain a value of $|\Lambda| \approx 2.9$; these values are typical of the materials used in many other experimental works, although not all of them document the material properties in detail.

To predict how the shape of the beam evolves with time, we solve these equations (12) and (13) for $\theta(S,T)$ using a numerical method described in the Supplementary Materials A with specific initial, boundary and illumination conditions. We remark that in deriving the equations, we assumed that the material response—the relation between curvature and moment (6), and the relation between illumination and spontaneous curvature (7)—are linear. Yet, the final equations are nonlinear as evidenced by the presence of the trigonometric terms in (12) and f in (13) due to the nonlinearity of the kinematics of large deformation and the presence of finite rotations.

For future reference, we note that the equilibrium equation (12) can be derived by the Euler-Lagrange method as the stationarity condition of the energy functional

$$\mathcal{E}[\theta] = \int_0^1 \frac{1}{2}\left|\frac{\partial\theta}{\partial S} - K_0\right|^2 \mathrm{d}S. \tag{15}$$

2 Rolling ring

Our first example is motivated by the work of Yamada *et al.* [12] on a rolling ring and motor, as well as that of Wei *et al.* [11] on a rolling spiral. We consider a closed, initially circular ring on a rigid horizontal surface, which is illuminated with a steady source at angle θ_I. The fact that the ring is closed implies that

$$\int_0^1 \sin\theta(S,T)\mathrm{d}S = \int_0^1 \cos\theta(S,T)\mathrm{d}S = 0, \tag{16}$$

as well as $\theta(0,T) = \theta(1,T)$. We assume that the ring makes a tangential rolling contact with the horizontal surface so that $X(S_c(T),T) = S_c(T)$, $Y(S_c(T),T) = 0$ and

$$\theta(S_c(T),T) = 0, \tag{17}$$

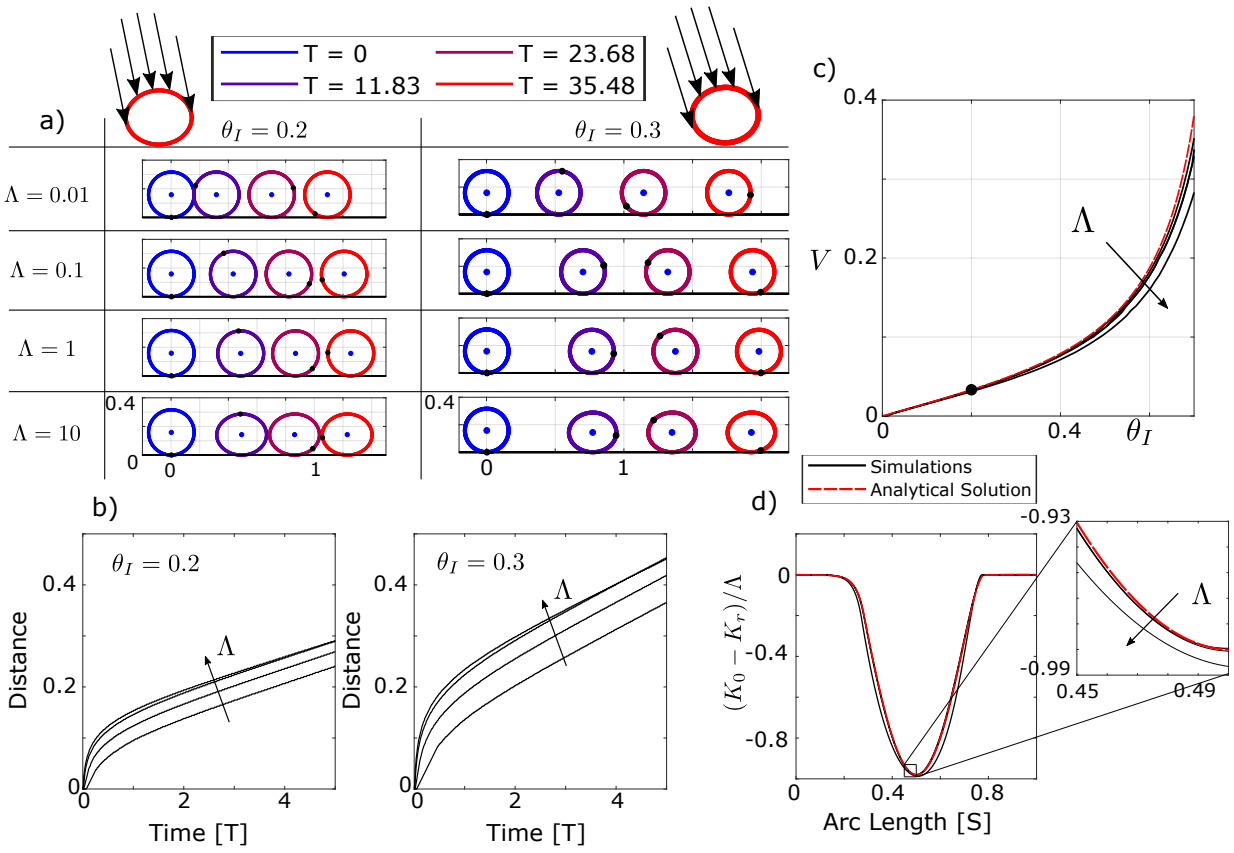

Figure 2: Rolling ring. (a) Snapshots of an initially circular ring with radius $R = 1/(2\pi)$ subjected to illumination at angle θ_I and of intensity Λ at times $T = \{0, 11.83, 23.68, 35.48\}$. The point that is initially in contact with the ground is marked with a black dot while the center of mass is the blue dot. The incident arrows indicate the direction of incoming light. Self-shadowing is taken into account thanks to the choice of f in equation (11); this is depicted by the absence of arrows in the lower part of the ring. (b) Distance traveled by the rolling ring vs. time for various intensities $\Lambda = \{0.01, 0.1, 1, 10\}$. Note that the a steady velocity is reached in all cases, after an initial transient. (c) Steady state velocity as a function of illumination angle and intensity. The velocity increases when the illumination angle moves away from the vertical, but is relatively insensitive to the intensity of illumination. (d) Scaled change of spontaneous curvature induced by illumination along the beam for $\theta_I = 0.2$ (indicated by dot in (c)), for various illumination intensities. This quantity appears to be largely insensitive to the intensity of illumination where Λ are as in (b). Simulation data is shown as solid black lines while the analytical solution given by solving Equation (29) is shown as a red dashed line.

where $S_c(T)$ is the point of contact. We determine this point of contact by assuming overall mechanical equilibrium of the ring under gravity so that the center of mass of the ring is always vertically above the point of contact,

$$\begin{aligned} S_c(T) = X(S_c(T),T) &= \int_0^1 X(S,T)\mathrm{d}S = \int_0^1 \left(\int_0^S \cos\theta(\tilde{S},T)\mathrm{d}\tilde{S}\right)\mathrm{d}S \\ &= \int_0^1 (1-S)\cos\theta(S,T)\mathrm{d}S = -\int_0^1 S\cos\theta(S,T)\mathrm{d}S. \end{aligned} \tag{18}$$

We set $K_r = 2\pi$ and $\theta(S,0) = 2\pi S$ corresponding to an initially circular ring and solve the equations (12), (13) subject to the conditions above. Figure 2(a) shows snapshots of the ring for various angles and intensity of illumination. In each case, the ring deforms as it is illuminated, in a way which is non-symmetric with respect to the vertical axis and depends on the angle of illumination. This asymmetry causes the center of mass of the ring to move, which in turn causes the ring to roll. Figure 2(b) shows the distance travelled by the point of contact as a function of time under various angles and intensity of illumination. After an initial transient, the ring rolls with a steady velocity and has an invariant shape. The steady velocity is plotted as a function of the illumination angle for various illumination intensities in Figure 2(c): it is zero when the illumination is vertical ($\theta_I = 0$), which is a consequence of the symmetry, and increases with increasing angle of illumination θ_I. Remarkably, *the rolling velocity is practically independent of the intensity of illumination* in the range of values of Λ relevant to the experiments and investigated here. To investigate this further, we plot the scaled deviation in spontaneous curvature $(K_0 - K_r)/\Lambda$ as a function of arclength in Figure 2(d): this quantity appears to be practically independent of the intensity of illumination as well. This shows that amount of deformation scales linearly with the light intensity, while the profile of deformation (and, hence, the asymmetry and the rolling velocity) is largely independent of the intensity.

To understand these features, we analyze steadily rolling solutions, *i.e.*, we seek solutions of the form $\theta(S,T) = \Theta(S - VT)$ and aim at identifying the rolling velocity V. We set $\omega = 2\pi(S - VT)$ choosing $T = 0$ to be a time when the point in contact with the ground is $S = S_c(0) = 0$. This implies

$$\Theta(0) = 0. \tag{19}$$

The rolling condition (18) becomes

$$0 = \int_0^{2\pi} \omega\cos\Theta(\omega)\mathrm{d}\omega, \tag{20}$$

and the evolution equation (13)

$$-2\pi V\frac{\mathrm{d}K_0}{\mathrm{d}\omega} + (K_0 - 2\pi) = \Lambda f(\Theta - \theta_I). \tag{21}$$

We now assume that *the shape of the ring is almost circular* so that

$$\Theta(\omega) = \omega + \Theta_1(\omega), \quad K_0(\omega) = 2\pi + K_1(\omega) \tag{22}$$

where $|\Theta_1| \ll 1$ and $|K_1| \ll 1$ are treated as perturbations. Keeping only terms linear in Θ_1, K_1, the equilibrium equation (12) and closure condition (16) become

$$\begin{aligned} &4\pi^2\Theta_1''(\omega) - 2\pi K_1'(\omega) + F_y\cos\omega - F_x\sin\omega = 0\,, \\ &\textstyle\int_0^{2\pi}\cos(\omega)\Theta_1(\omega)\mathrm{d}\omega = \int_0^{2\pi}\sin(\omega)\Theta_1(\omega)\mathrm{d}\omega = 0\,. \end{aligned} \tag{23}$$

Introducing the Fourier transform $\hat{f}(k) = \int_0^{2\pi} f(\omega)\exp(-ik\omega)\mathrm{d}\omega$ where k is an integer, we can solve (21) as

$$\hat{K}_1(k) = \frac{\Lambda \hat{f}_I(k)}{1 - 2i\pi kV}\,, \tag{24}$$

where

$$f_I(\omega) = f(\omega - \theta_I). \tag{25}$$

Similarly, we can solve equation (23) in Fourier form as

$$\begin{array}{rcll} \hat{\Theta}_1(\pm 1) & = & 0 & \text{for } |k| = 1, \\ \hat{\Theta}_1(k) & = & -i\frac{\hat{K}_1(k)}{2\pi k} & \text{for } |k| \geqslant 2. \end{array} \tag{26}$$

Note that the first equation in (23) yields F_x and F_y in terms of $\hat{\Theta}_1(\pm 1)$ and $\hat{K}_1(\pm 1)$ as well, but these expressions are not needed.

The horizontal tangency condition (19) reads $0 = \Theta(0) = \Theta_1(0) = \frac{1}{2\pi}\sum_k \hat{\Theta}_1(k)$ where the sum runs over all *signed* integers k. Rearranging the terms in the sum and solving for $\hat{\Theta}_1(0)$, we find

$$\hat{\Theta}_1(0) = -2\sum_{k\geqslant 1} \mathrm{Re}\,\hat{\Theta}_1(k) \tag{27}$$

where we have used $\hat{\Theta}_1(-k) + \hat{\Theta}_1(k) = \overline{\hat{\Theta}_1(k)} + \hat{\Theta}_1(k) = 2\,\mathrm{Re}\,\hat{\Theta}_1(k)$ since $\Theta_1(\omega)$ is a real function. Here, $\overline{z}$ denoting the conjugate of the complex number z.

Equations (24–27) yield the shape in terms of the known illumination parameter Λ and of the unknown scaled rolling velocity V. The latter can be found by linearizing the rolling condition (20) as $\int_0^{2\pi} g(\omega)\Theta_1(\omega)d\omega = 0$ where $g(\omega) = \omega\sin\omega$. Using Parseval's identity, this can be rewritten as

$$\frac{1}{2\pi}\sum_k \hat{g}(k)\hat{\Theta}_1(-k) = 0, \qquad \text{where } \hat{g}(k) = \begin{cases} -\frac{\pi}{2}(2\pi ik + 1) & \text{if } |k| = 1\,, \\ \frac{2\pi}{k^2-1} & \text{if } |k| \neq 1\,. \end{cases} \tag{28}$$

Inserting (26–27) into this equation, we obtain $2\sum_{k\geqslant 2}\frac{k^2}{k^2-1}\,\mathrm{Re}\,\hat{\Theta}_1(k) = 0$ which, in view of (24–26), yields an implicit equation for the rolling velocity V in terms of the angle of illumination θ_I,

$$\Lambda \cdot H(\theta_I, V) = 0 \quad \text{where} \quad H(\theta_I, V) = \sum_{k\geqslant 2}\frac{k}{k^2-1}\,\mathrm{Im}\left(\frac{\hat{f}_I(k)}{1 - 2i\pi kV}\right). \tag{29}$$

Note that f_I and hence H depends on θ_I, see equation (25).

When $\theta_I = 0$, $f_I(\omega) = f(\omega)$ is an even function of ω, so that $\hat{f}_0(k)$ is real, hence $H(0,0) = 0$. It is also clear from the form of $H(\theta_I, V)$ that $\dfrac{\partial H}{\partial \theta_I}$ and $\dfrac{\partial H}{\partial V}$ are generally non-zero. By the implicit function theorem, we can solve (29) for $V = V(\theta_I)$, at least for θ_I small enough. We do so numerically; the result is shown in Figure 2(c) as the dashed line, and agrees well with the non-linear simulations. In Figure 2(d), the distribution of natural curvatures predicted by the linear theory is compared to the non-linear numerical simulations, and a good agreement is obtained as well; the agreement with the linear theory is better and better for lower and lower illuminations, as could be anticipated.

Remarkably, the intensity of illumination Λ factors out in equation (29) selecting the rolling velocity, so that V depends on θ_I but not on Λ in this linear theory: this explains why the rolling velocity is largely independent of Λ in the non-linear simulations.

3 Waves in doubly clamped beams

The second example we study is motivated by the experiments of Gelebart *et al.* [4]. These experiments were done on a nematic strip possessing a splay director field: the nematic directors are aligned along the length of strip on one surface (called the *planar face*) and normal to the surface on the opposite face (*homeotropic face*). The goal is to induce contraction on one face and expansion on the other in order to maximize the magnitude of the photo-bending coupling $|\lambda|$. Exposing the planar face to light makes $\lambda < 0$ while exposing the homeotropic face to light makes $\lambda > 0$. In view of the analysis done in Section 1, $\Lambda \propto \alpha \propto -\lambda$, so illuminating the planar (respectively, homeotropic) face corresponds to $\Lambda > 0$ (resp. $\Lambda < 0$) in our model. Illumination, either due to the direct effect or due to temperature rise or both, reduces the nematic order causing a contraction by $(r/r_0)^{2/3}$ when illuminated on the planar face and an extension by $(r_0/r)^{1/3}$ when illuminated on the homeotropic face where r (respectively r_0) is the anisotropy parameter in the illuminated (respectively ambient) state. Since $r < r_0$, for fixed unscaled illumination intensity I_0, we expect the resulting photo-strain and spontaneous curvature coefficients $0 \leq \Lambda_p \approx -2\Lambda_h$, where Λ_p is the coefficient when illuminated on the planar side and Λ_h when illuminated on the homeotropic side. This distinction between Λ_p and Λ_h is caused by the small penetration depth only activating the *trans* to *cis* isomerization on the illuminated side; therefore, it is only the nematic orientation on the illuminated surface that matters. We study the results of our model first, and compare to the experimental observations next.

We first consider the case $\Lambda > 0$. We take a strip that is flat in the absence of any light or stress, so that $K_r = 0$. We use the same scaled quantities as earlier, and the scaled length of the strip is 1. We clamp the two ends at a distance $l_f < 1$ from each other, corresponding to boundary conditions

$$\theta(0,T) = \theta(1,T) = 0, \quad \int_0^1 \sin\theta(S,T)\mathrm{d}S = 0\,, \quad \int_0^1 \cos\theta(S,T)\mathrm{d}S = l_f. \tag{30}$$

Since $l_f < 1$, the beam buckles and there are two equivalent fundamental buckled modes, buckled up and down. We choose one of the two states, say the buckled up state for definiteness, although the results are independent of this choice. We illuminate the strip with a light source that is spatially uniform and at an angle ($\theta_I \neq 0$) as shown in Figure 3(a). We solve the equations (12–13) subject to the boundary conditions (30).

Figure 3(a-e) show a typical simulation result. After an initial transient, we find that the beam goes into a periodic motion alternating between the up and down buckled shapes, see Figure 3(a). At the start of the cycle, we have an up-bump at the left side of the strip (state A). Illumination moves it to the right initially rapidly but slowing down and becoming very slow as it reaches the right end (B). It then pops into a down bump located on the left (C). Subsequently, the down-bump moves to the right initially rapidly but slowing down and becoming very slow as it reaches the right end (D). It then pops again into up-bump located on the left of the sample, and the cycle repeats.

The evolution of the light-induced spontaneous curvature as a function of time and position is shown in Figure 3(b). After an initial transient, we see that the spontaneous curvature reaches a steady periodic cycle. This is emphasized in Figure 3(c), which plots one particular Fourier component $\gamma(T)$ of the deflection, against one particular Fourier component $\beta(T)$ of the natural curvature,

$$\gamma(T) = \int_0^1 \sin(2\pi S)Y(S,T)\mathrm{d}S\,, \quad \beta(T) = \int_0^1 \sin(2\pi S)K_0(S,T)\mathrm{d}S. \tag{31}$$

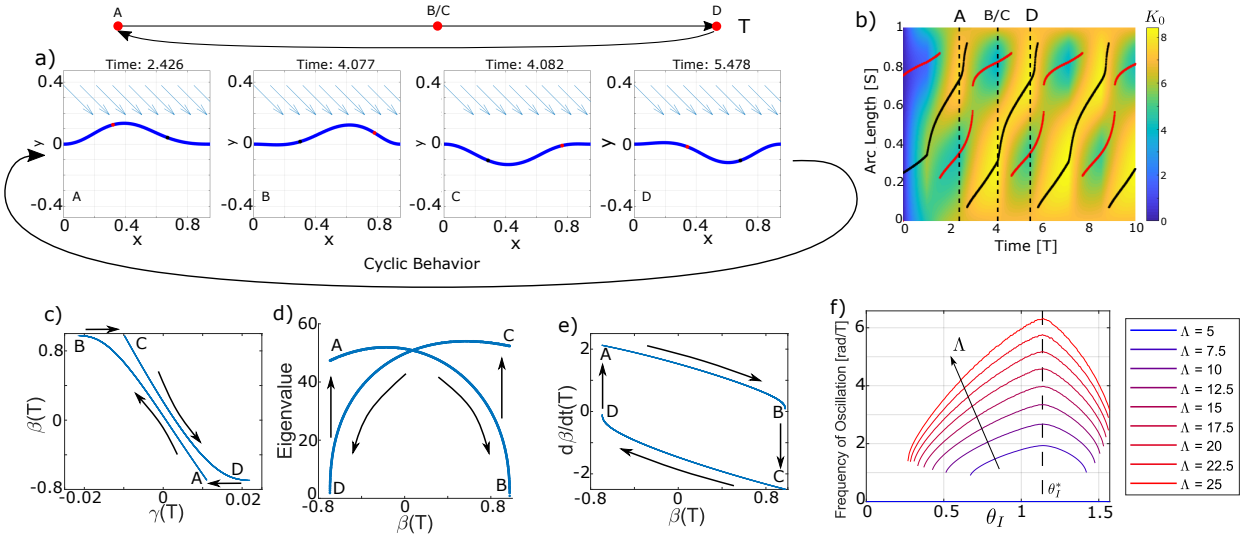

Figure 3: Waves in a strip for $\Lambda > 0$. (a) Snapshots of an initially flat strip clamped in a buckled state ($l_f = 0.95$) and subjected to illumination with $\Lambda = 10, \theta_I = \pi/4$. The arrows indicate the direction of incoming light. After an initial transient, it goes into a periodic motion. (b) Evolution of the light-induced spontaneous curvature K_0 of the strip. The peaks are marked with a black curve and the troughs are marked with a red curve. Note that the evolution becomes periodic but is quite complex with an alternation of slow (quasi-static) and fast (dynamic) motions. (c) Shape vs. spontaneous curvature descriptors as defined in Equation (31). (d) Incremental stiffness (lowest eigenvalue of the stiffness matrix) vs. spontaneous curvature descriptor. (e) Phase plot revealing the oscillation cycles after an initial transient. (f) Frequency of flapping as a function of illumination angle for various illumination angles. The angle for maximum flapping frequency (θ_I^*) is shown with the vertical dashed line.

We call these quantities the descriptors of the deformation and curvature, respectively. In the figure, the deformation descriptor appears to vary abruptly during the sudden changes from state B to C, and from D to A, although the the curvature descriptor remains unchanged. This suggest that the jumps are snap-through bifurcations, from one equilibrium solution of the elastica to another one. For some fixed time T and spontaneous curvature distribution $K_0(S,T)$, the equilibrium equation (12) may have multiple solutions (equivalently, $\mathcal{E}$ has multiple stationary points). Stable solutions are those for which the second variation is positive definite (Supplementary Material B). With the aim to confirm the snap-through scenario, we study the lowest eigenvalue associated with the second variation $\delta^2\mathcal{E}$ of the energy. It is plotted from the numerical solution, as a function of β in Figure 3(d). We see that this eigenvalue is positive at the start of the cycle at A (the solution with the up-bump) but decreases as we go from A to B. The jump at B occurs when the eigenvalue is becoming negative and the solution loses stability. It arrives on another solution C having a down-bump, which appears to be elastically stable, *i.e.*, has a positive lowest eigenvalue. Again, the lowest eigenvalue begins to decrease as we go from C to D and passes through zero at D.

This reveals the mechanism of the cyclic motion. At any time, there are two possible solutions, one with an up-bump and one with a down-bump. If the solution with the up-bump has the bump on right, the solution with the down-bump has the bump on the left and vice-versa. The evolution of light-induced spontaneous curvature always forces the bump to move to the right, *i.e.*, away from the light source. At some point it loses stability and has to snap to the other solution. The periodic cycles are represented in the phase space $(\beta, \dot{\beta})$ in Figure 3(e). Immediately after a snap-through, the evolution speed $|\dot{\beta}|$ is high. As the instability is approached, the magnitude of $|\dot{\beta}|$ decreases until nearly zero. This coincides with the snap through and once the system snaps to the new configuration, $|\dot{\beta}|$ jumps to a large value again, and the other half of the cycle proceeds similarly.

We repeat this calculation for various illumination angles and illumination intensities, and the results are summarized in Figure 3(f). At any given intensity, there is a window of illumination angles at which periodic flapping solutions are observed. Outside this window, a stationary solution is reached, which can be the up-bump or the down-bump depending on the initial conditions. Physically, if the illumination is oriented in a direction too shallow to the beam, then the bump moves to the far end and is stable. This explains the lower limit. Similarly, if the illumination is close to being normal to the beam, then the beam finds it difficult to break the symmetry required to induce the periodic motion. This explains the upper limit. The window of periodic behavior becomes wider when the light intensity is increased. Further, at any given orientation, the frequency of the limit cycle increases with intensity; this can be seen from equation (10), where an increase of the light intensity in the right-hand side is seen to induce a quicker rate of change $\partial\kappa_0/\partial t$ of the curvature.

In figure 3(f), the angle of incidence θ_I maximizing the flapping frequency is 65.1° for $l_f = 0.95$, and this angle appears to be virtually independent of the light intensity as long as flapping takes place: it is just a function of l_f in our model. To compare with the observations of [4], we ran additional simulations using the same value $l_f = 0.957$ as in the experiments, and found that the maximum frequency is obtained for an angle of incidence $\theta_I = 65.7^\circ$; this value is similar to the peak at 70° in the experiment.

We now turn to the case when $\Lambda < 0$. As can be seen in Figure 4(a), the system again alternates between up and down buckled states. In this case, however, the bulge propagates from right to left, *i.e.*, towards the light source, and opposite from the case where $\Lambda > 0$. It can be seen in (c)–(e) that the descriptors give different paths through the phase space than when $\Lambda > 0$. This shows

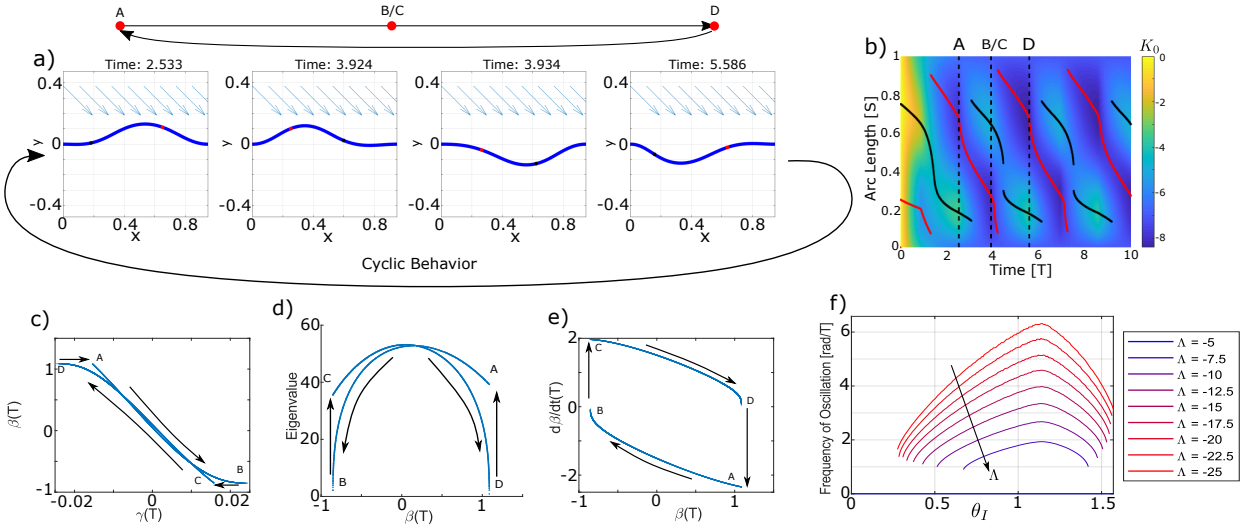

Figure 4: Waves in a strip for $\Lambda < 0$. Same as in Figure 3 except with $\Lambda = -10$.

that flipping the sign of Λ does not simply amount to reverse the arrow of time. Interestingly, even though the deformation mode differs, the flapping frequency (f) does not change significantly between the positive and negative cases.

We now compare the experimental observations of Gelebart *et al.* [4]. After an initial transient, the strip begins a periodic motion with the wave moving from right to left as predicted in Figure 4, when illuminated on the homeotropic phase ($\Lambda = \Lambda_h < 0$). The wave moves from left to right as predicted in Figure 3 when illuminated on the planar face ($\Lambda = \Lambda_p > 0$). They also observed that the frequency of oscillation when illuminating the homeotropic face is lower as compared to the planar face, holding all other parameters fixed. Again, this is consistent with the predictions in Figures 4(f) and 3(f) since $|\Lambda_p| > |\Lambda_h|$ for fixed I_0. Further, this wave-like motion is observed only in a finite range of illumination angles and, for fixed illumination intensity, the range when illuminating the planar side is larger than that of the homeotropic side as predicted because $|\Lambda_p| > |\Lambda_h|$. All these results are in good agreement with the experimental observations.

4 Snap-through instability of doubly clamped beams

The critical event in the emergence of wave-like cyclic behavior is the snap-through instability. We study this instability more closely in our final example, by analyzing the experiments first conducted by Shankar and collaborators [6, 7].

As in the previous example, an initially flat ($K_r = 0$) strip of (normalized) length 1 is clamped at both ends so that the end to end distance is $l_f < 1$; the beam is subject to the same boundary conditions (30). There are two equilibrium conditions, one buckled up, and one buckled down. As before, we start with the buckled up state and shine light on it. There are two differences compared to the geometry of the previous section: we limit attention to normal illumination ($\theta_I = 0$), and use a wide light beam described by a Gaussian distribution of intensity:

$$\Lambda(S,T) = \Lambda_{\max}\, g(X(S,T), \mu, W)\,, \tag{32}$$

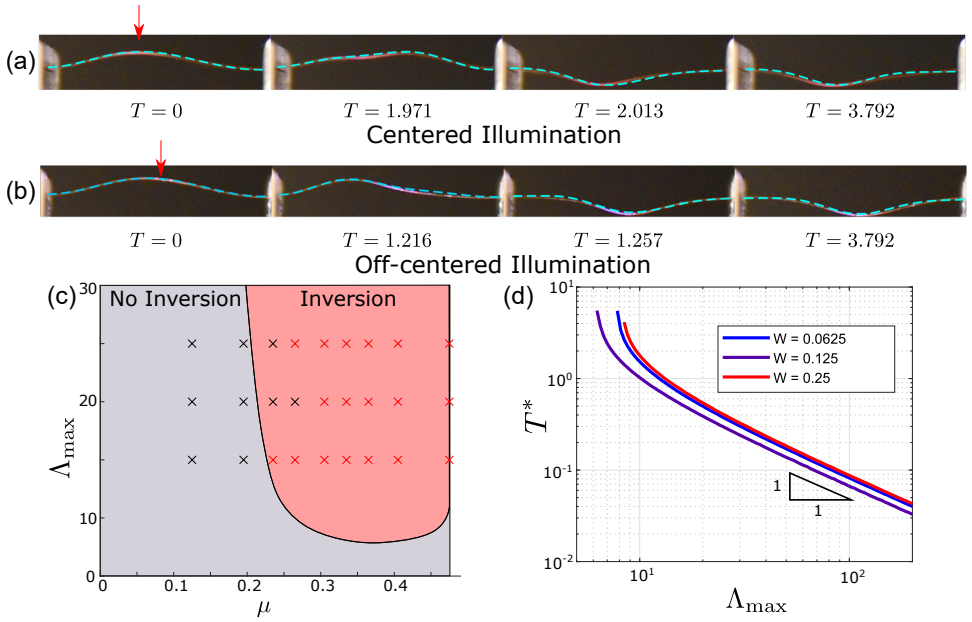

Figure 5: Snap-through of a strip subject to normal illumination. (a,b) Snapshots of an initially flat strip clamped in a buckled state and subjected to illumination with $\Lambda_{\max} = 10$ and $l_f = 0.99$ for two different offsets, (a) $\mu = l_f/2$ and (b) $\mu = 0.45$. The red arrows indicate the location of the center of the laser beam. Predictions of the model (cyan) are superimposed onto the experimental observations without any adjustable parameter. Note the two distinct snap-through modes: symmetric with the creation of a flat-top when the light beam is centered and displacing the peak position when the light beam is not centered. (c) Phase portrait in the illumination vs. offset plane, showing the absence or presence of snap-through, for $l_f = 0.95$. The background colors and the crosses are the theoretical and experimental results, respectively. (d) Time for snap-through as a function of illumination for $l_f = 0.95$ and $\mu = l_f/2$, as predicted by the model.

where $g(X, \mu, W) = \exp\left(-\frac{(X-\mu)^2}{2W^2}\right)$ is a normal distribution centered at μ, with width W and scaled so that the peak value is 1.

We also conduct experiments using 1mm × 15mm × 50 μm beams made of planar nematic LCN films (see Materials and Methods and Supplementary Materials C for details) illuminated using a 365 nm LED.

Figure 5 summarizes our results. First consider the case when the illumination is centered on the bump ($\mu = l_f/2$) in Figure 5(a). When the light is turned on, the bumps flattens out slowly due to photo-induced curvature; after a period of slow deformation, it snaps suddenly at a critical time T^* to the down-buckled state. We have verified through eigenvalue analysis as before that the snap-through occurs when the up-bump solution becomes unstable. Continued illumination beyond the time of snap-through does not result in any significant further deformation. Figure 5(b) shows the results of the case where the illumination is slightly off the center of the bump ($\mu = 0.45$). The overall phenomenon is similar, but the initial slow deformation pushes the bump to the side away from the illumination instead of flattening it. These figures Figure 5(a,b) superpose the results of theoretical computation (cyan dashed line) with images retrieved from the experimental

observation, showing excellent agreement.

As the illumination becomes too low, or the off-set from center $|l_f/2 - \mu|$ is too large, the beam does not snap-through. The phase portrait is shown in Figure 5(c) along with the experimental observations, again showing good agreement between theory and experiments. At higher illuminations, we see some evidence of photo-bleaching in the experiments and we believe that this accounts for the slight discrepancy. The phase portrait also shows that the smallest illumination required for snap-through decreases as the light is moved away from the center (i.e., when μ decreases from $l_f/2$). In other words, it is easier to snap when the illumination is slightly off center.

Finally, the time it takes for the snap-through to occur as a function of illumination in the centered case is plotted in Figure 5(d). We observe that for moderate to large illumination (i.e., away from the snap/no-snap boundary), this takes on a power law with an exponent -1. Shankar *et al.* [6] had studied this over a very large range of illuminations, and they reported a slope of -1, in agreement with our simulations.

Materials and Methods

Planar nematic liquid crystal network films were prepared following the procedure of Gelebart *et al.* [4] with modification. To synthesize films with a a penetration depth of 1.5 μm at an illumination wavelength of 365 nm, a formulation of 9.2 : 90.8 by weight of 4,4'-Bis(6-acryloyloxyhexyloxy)azobenzene (Azo-6) : 1,4-Bis[4-(6-acryloyloxyhexyloxy)benzoyloxy]-2-methylbenzene (RM82) was used, with 2.5 wt% of photoinitiator with respect to the total monomer weight. In a typical sample preparation, 4.6 mg Azo-6, 45.4 mg RM82, and 1.25 mg Iphenylbis(2,4,6-trimethylbenzoyl)phosphine oxide) (Irgacure 819) were melted together in a vial and vortexed repeatedly to ensure mixing. The molten monomer mixture was then infiltrated via capillary action into alignment cells on a hot plate at 100°C. The alignment cells were prepared by spin-coating Elvamide onto clean glass slides, rubbing the slides with a velvet cloth, and gluing the two Elvamide sides facing each other with epoxy mixed with 15 μm glass beads. The filled cells were subsequently cooled to 80°C, held isothermal for 5 minutes to induce alignment of the liquid crystalline mesogens, and photopolymerized for 30 minutes with 405 nm light. Following photopolymerization, samples were post-cured at 120°C for 10 minutes and the 15m thick LCNs were harvested by cracking open the alignment cells with a razor blade. Finally, beams of 1 mm in width were cut from the film with the nematic director along the long axis of the strip.

Acknowledgement This work started while BA visited Caltech as a Moore Distinguished Scholar in 2017-18. KK, AK, KB, RH gratefully acknowledge the support of the US Office of Naval Research through the MURI grant ONR N00014-18-1-2624. KK also acknowledges the support of the National Science Foundation Graduate Research Fellowship under Grant No. DGE-1745301.

Author contributions KK, BA and KB worked on the theoretical formulation. KK performed the numerical simulations with supervision from BA and KB. AK conducted the experiments with supervision from RH. KK, BA and KB took the lead in writing the manuscript with final edits from all authors.

References

[1] Tian Chen, Osama R Bilal, Kristina Shea, and Chiara Daraio. Harnessing bistability for directional propulsion of soft, untethered robots. *Proceedings of the National Academy of Sciences*, 115(22):5698–5702, 2018.

[2] D Corbett and M Warner. Nonlinear Photoresponse of Disordered Elastomers. *Physical Review Letters*, 96(23):237802, June 2006.

[3] Daniel Corbett, Chen Xuan, and Mark Warner. Deep optical penetration dynamics in photobending. *Physical Review E*, 92(1):013206, July 2015.

[4] Anne Helene Gelebart, Dirk Jan Mulder, Michael Varga, Andrew Konya, Ghislaine Vantomme, E. W. Meijer, Robin L. B. Selinger, and Dirk J. Broer. Making waves in a photoactive polymer film. *Nature*, 546:632–636, June 2017.

[5] Yin Lin, Lihua Jin, and Yongzhong Huo. Quasi-soft opto-mechanical behavior of photochromic liquid crystal elastomer: Linearized stress–strain relations and finite element simulations. *International Journal of Solids and Structures*, 49(18):2668 – 2680, 2012.

[6] M. Ravi Shankar, Matthew L. Smith, Vincent P. Tondiglia, Kyung Min Lee, Michael E. McConney, David H. Wang, Loon-Seng Tan, and Timothy J. White. Contactless, photoinitiated snap-through in azobenzene-functionalized polymers. *Proceedings of the National Academy of Sciences*, 110(47):18792–18797, 2013.

[7] Amir Alipour Skandani, Sourav Chatterjee, Matthew L. Smith, John Baranski, David H. Wang, Loon-Seng Tan, Timothy J. White, and M. Ravi Shankar. Discrete-state photomechanical actuators. *Extreme Mechanics Letters*, 9:45 – 54, 2016.

[8] Matthew L. Smith, M. Ravi Shankar, Ryan Backman, Vincent P. Tondiglia, Kyung Min Lee, Michael E. McConney, David H. Wang, Loon-Seng Tan, and Timothy J. White. Designing light responsive bistable arches for rapid, remotely triggered actuation. *Behavior and Mechanics of Multifunctional Materials and Composites 2014*, 9058(March 2014):90580F, 2014.

[9] Timothy J White. *Photomechanical Materials, Composites, and Systems.* Wireless Transduction of Light into Work. John Wiley & Sons, May 2017.

[10] Timothy J White, Nelson V Tabiryan, Svetlana V Serak, Uladzimir A Hrozhyk, Vincent P Tondiglia, Hilmar Koerner, Richard A Vaia, and Timothy J Bunning. A high frequency photodriven polymer oscillator. *Soft Matter*, 4(9):1796–3, 2008.

[11] Jeong Jae Wie, M. Ravi Shankar, and Timothy J. White. Photomotility of polymers. *Nature Communications*, 7:13260, November 2016.

[12] Munenori Yamada, Mizuho Kondo, Jun-ichi Mamiya, Yanlei Yu, Motoi Kinoshita, Christopher J. Barrett, and Tomiki Ikeda. Photomobile polymer materials: Towards light-driven plastic motors. *Angewandte Chemie International Edition*, 47(27):4986–4988, March 2008.

[13] Yanlei Yu, Makoto Nakano, and Tomiki Ikeda. Photomechanics: Directed bending of a polymer film by light. *Nature*, 425:145, 2003.

Supplementary Material

Movie S1 (Separate file). Transient behavior of rolling ring in the presence of illumination. Results are shown for $\theta_I = 0.2$ and $\theta_I = 0.3$ at various intensities of illumination.

Movie S2 (Separate file). Transient behavior of flapping beam in the presence of illumination. Results are shown for $\theta_I = \pi/4$ and various intensities of illumination. The top row is the case when $\Lambda > 0$ and the bottom row is when $\Lambda < 0$

A Computational Model

The numerical method is motivated by the discrete elastic rod model[1]. We partition the beam into $N-1$ segments $\mathcal{S}^i = (S_i, S_{i+1}),\ i = 1, \ldots, N-1$ which are all equal in arc-length by introducing N nodes: the ith node is at arc-length $S_i = (i-1)L/(N-1)$. We introduce the angle $\theta^i,\ i = 1, \ldots, N-1$ to be the angle that the segment $\mathcal{S}^i$ makes to the horizontal as our main kinematic variable. We can then obtain the current position of the nth node by exploiting the inextensibility condition as follows:

$$\mathbf{x}_n = \mathbf{x}_1 + \sum_{i=2}^{n} (S_i - S_{i-1}) \left(\cos\theta^{i-1}\mathbf{e}_1 + \sin\theta^{i-1}\mathbf{e}_2 \right).$$

The curvature is carried at the nodes and defined as $\kappa_i = \theta^i - \theta^{i-1}$ so that the total bending energy of the beam (discrete equivalent to (15)) is given by

$$E_B[\theta] = \sum_{i=2}^{N-1} \frac{1}{2} J_i (\theta^i - \theta^{i-1} - \kappa_i^0)^2 \tag{33}$$

where J_i is a bending modulus and κ_i^0 is the discrete natural curvature at the ith node.

We obtain the equilibrium equation (discrete equivalent to (12)) by taking the variation of E_B with respect to θ^j:

$$\frac{\partial E_B}{\partial \theta^j} = J_j(\theta^j - \theta^{j-1} - \kappa_j^0) - J_{j+1}(\theta^{j+1} - \theta^j - \kappa_{j+1}^0) = 0. \tag{34}$$

Given the spontaneous curvatures $\{\kappa_j^0\}$, we solve these equations for $\{\theta^j\}$ subject to appropriate boundary conditions. In order to improve the stability and convergence, it is convenient to have the Hessian,

$$\frac{\partial^2 E_B}{\partial \theta^j \partial \theta^k} = -J_j \delta_k^j + (J_j + J_{j+1})\delta_k^j - J_{j+1}\delta_k^{j+1}.$$

It remains to specify the spontaneous curvature. This evolves according to (13) whose discrete version is given by the set of ordinary differential equations:

$$\frac{\mathrm{d}\kappa_i^0}{\mathrm{d}t} + \kappa_i^0 = \Lambda f(\theta_i - \theta_I), \tag{35}$$

[1] Miklós Bergou, Max Wardetzky, Stephen Robinson, Basile Audoly, and Eitan Grinspun. Discrete elastic rods. *ACM Transactions on Graphics*, 27(3):63:1 – 63:12, August 2008.

where $f(\theta_i - \theta_I)$ is as defined in Equation 13 and $\theta_i = (ave)(\theta^i, \theta^{i-1})$ is defined as the angle of the tangent of the ith node.

Equation (35) is discretized in time using an explicit Newton time stepping algorithm. Time dependent solutions are obtained by alternating the elastic relaxation in equation (34) and evolving of natural curvatures κ_i^0 based on equation (35) over a time step.

A.1 Elastic Ring

In Section 2, we analyzed rolling rings. They can be simulated by adapting the general numerical procedure outlined above as follows. The closure of the ring is imposed by the following constraints:

$$\theta^1 = 0 \qquad \mathbf{x}_1 = \mathbf{x}_{N-1} \qquad \mathbf{x}_2 = \mathbf{x}_N$$

The first of these can be implemented explicitly by freezing that degree of freedom and represents that the point of contact is tangent to the surface.

The last two enforce the closure constraint. The system is initialized by assuming a constant curvature which makes the last two nodes coincident with the first two. Then the system is relaxed by minimizing the energy while imposing the constraints. In order to stabilize the point of contact when the system is circular, a small amount of gravity is initially added and removed once the natural curvature deviates from its initial state.

The algorithm for calculating the translation and rotation of the system is as follows. Initially, the point of contact is defined to be the first and second nodes (second to last and last due to constraints). Then, given a natural curvature, κ_j^0, the energy is minimized to find the new configuration. The natural curvature is then updated using the explicit forward Euler scheme according to (35). Then, using a small window near the first and second nodes (which wraps around to nodes on the far end of the beam), the closest node to the calculated center of mass is found. Then, the nodes on either side of that node are tested to find the closest to the center of mass. This then forms an ordered pair of nodes $(\mathbf{x}_i, \mathbf{x}_{i+1})$ which defines the segment closest to the center of mass. Then, by shifting the minimized curvature $\theta^i \to \theta^1$, $\theta^{i+1} \to \theta^2$, etc in a cyclic manner (so the quantities at end points get wrapped around the beam). Similar transformations are done to the natural curvature ($\kappa_i^0 \to \kappa_{N-1}^0$, $\kappa_{i+1}^0 \to \kappa_2^0$). Note that these transformations are done in such a way that the ordering of the nodes is preserved and wrapped. At this point, the updated points of contact are now the 1st and 2nd nodes and the algorithm can be repeated to integrate the system in time. This solves for the rotation of the system while the translation can be found by using the rolling contact condition. Using the convention before, we had set $\mathbf{x}_1 = \mathbf{0}$. We can set this to be the relative position where the true position of node i is defined as $\tilde{\mathbf{x}}_i = \mathbf{x}_{S_c} + \mathbf{x}_i$ where $\mathbf{x}_{S_c}$ is the position of the point of contact. $\mathbf{x}_{S_c}$ is found using the rolling condition. Let $\mathbf{x}_{S_c}^k$ be the position of the point of contact at time step k and i be the shift necessary to establish that the point of contact is vertically aligned with the center of mass. Then,

$$\mathbf{x}_{S_c}^{k+1} = \begin{cases} \mathbf{x}_{S_c}^k + (S_i - S_1)\mathbf{E}_1 & \text{if } i \in [1, Ns] \\ \mathbf{x}_{S_c}^k + (S_i - S_{N-1})\mathbf{E}_1 & \text{if } i \in [N - Ns, N-1] \end{cases},$$

where N_s is a small window (usually set to $N/20$). If i is not in the range of values defined above, then the time discretization is made finer in order to ensure that the rotations induced in each time step correlate with a small translation. The results for various angles of incidence of light and intensities are given in Movie S1 in the supplementary material. The "velocity" of the system is

then found by finding the distance the point of contact travels over a small time window. Steady state velocities are found by iterating the time stepping procedure until the velocity reaches a steady value.

A.2 Doubly Clamped Beam

The doubly clamped system can be solved by setting up the following constraints

$$\theta^1 = 0 \qquad \theta^{N-1} = 0 \qquad \mathbf{x}_N = l_f \mathbf{e}_1$$

where $l_f < L$ is the distance between the two endpoints. As before, the first of these two constraints can be implemented explicitly by freezing those degrees of freedom and requires no special treatment, while the latter two constraints need to be implemented in the optimization engine. The initial solution is obtained numerically by decreasing l_f from 1 to its actual value in small steps. The system is integrated in time by alternating between relaxing the elastic energy and updating the natural curvature using an explicit Newton time stepping method. The results for various angles of incidence of light and intensities are given in Movie S2 in the supplementary material.

B Equilibrium and Stability Analysis

Investigation of the snapping instabilities from Section 3 requires obtaining the second variation of the energy $\mathcal{E}(\theta)$ in the presence of m constraints $c_i(\theta) = 0$, $i = 1, 2, ..., m$, where $\theta \in \mathbb{R}^n$ is the set of degrees of freedom. Denote the feasible set $\mathcal{C} = \{\theta \in \mathbb{R}^n \text{ s.t. } c_i(\theta) = 0\}$. We are interested in solutions $\bar{\theta} \in \mathcal{C} \subset \mathbb{R}^n$ such that

$$\mathcal{E}\left(\bar{\theta} + \varepsilon u + \frac{1}{2}\varepsilon^2 w\right) \geq \mathcal{E}(\bar{\theta}), \quad \forall u, w \in \mathbb{R}^n$$

satisfying $\bar{\theta} + \varepsilon u + \frac{1}{2}\varepsilon^2 w \in \mathcal{C}$, with $\varepsilon \to 0$. Expanding each of these out to first order and simplifying gives,

$$\nabla \mathcal{E}(\bar{\theta}) \cdot u = 0\,,$$
$$\nabla c_i(\bar{\theta}) \cdot u = 0\,.$$

where ∇ denotes the gradient operator relative to the degrees of freedom of the function ($(\nabla E)_i = \frac{\partial E}{\partial \theta_i}$). This gives the equilibrium condition,

$$\nabla \mathcal{E}(\bar{\theta}) + \sum_{i=1}^{m} \lambda_i \nabla c_i(\bar{\theta}) = 0,$$

where the parameters λ_i are Lagrange multipliers.

For stability, we require that any perturbation which satisfies the constraints will increase the energy. To do this, we expand our system to second order in ε and simplify:

$$u \cdot \nabla^2 \mathcal{E}(\bar{\theta}) u + \nabla \mathcal{E}(\bar{\theta}) \cdot w \geq 0\,,$$
$$u \cdot \nabla^2 c_i(\bar{\theta}) u + \nabla c_i(\bar{\theta}) \cdot w = 0\,,$$

where ∇^2 is the Hessian operator which returns the symmetric matrix of second derivatives. Using the equilibrium condition, we have

$$\nabla \mathcal{E}(\bar{\theta}) \cdot w = -\sum_{i=1}^{m} \lambda_i \nabla c_i(\bar{\theta}) \cdot w = u \cdot \sum_{i=1}^{m} \lambda_i \nabla^2 c_i(\bar{\theta}) u \,.$$

Plugging this into the above inequality, we have the stability condition that

$$u \cdot \left(\nabla^2 \mathcal{E}(\bar{\theta}) + \sum_{i=1}^{m} \lambda_i \nabla^2 c_i(\bar{\theta}) \right) u \geq 0 \,,$$

for all u such that

$$\nabla c_i(\bar{\theta}) \cdot u = 0 \,.$$

To determine whether a configuration satisfies this condition, we want to project $\mathbb{R}^n$ onto the space tangent to the constraints. This is done by a Gram-Schmidt process where

$$v_1 = \frac{\nabla c_1(\bar{\theta})}{\|\nabla c_1(\bar{\theta})\|} \,,$$

$$v_k = \frac{\nabla c_k(\bar{\theta}) - \sum_{i=1}^{k-1} (\nabla c_k(\bar{\theta}) \cdot v_i) v_i}{\|\nabla c_k(\bar{\theta}) - \sum_{i=1}^{k-1} (\nabla c_k(\bar{\theta}) \cdot v_i) v_i\|} \,,$$

$$P = I - \sum_{i=1}^{m} v_i \otimes v_i \,.$$

The stability analysis then boils down to calculating the eigenvalues of $P \left(\nabla^2 \mathcal{E}(\bar{\theta}) + \sum_{i=1}^{m} \lambda_i \nabla^2 c_i(\bar{\theta}) \right) P$. Due to the projection, there will be m zero eigenvalues and stability is implied when all other eigenvalues are greater than zero. This analysis determines if there exists feasible paths which locally lowers the energy; therefore, the existence of a non-positive eigenvalue implies a loss of stability of the configuration.

C Experimental Methods

Materials The monomers 1,4-Bis[4-(6-acryloyloxyhexyloxy)benzoyloxy]-2-methylbenzene (RM82) and 4,4'-Bis(6-acryloyloxyhexyloxy)azobenzene (Azo-6) were purchased from Synthon Chemicals and the photoinitiator phenylbis(2,4,6-trimethylbenzoyl)phosphine oxide) (Irgacure 819) was purchased from Sigma Aldrich. All chemicals were used as received. The polyimide alignment layer Elvamide was donated by Dupont.

Synthesis of LCN Beams Planar nematic LCN films were prepared following the procedure of Gelebart et al. (1) with modification. To synthesize films with the a penetration depth at 365 nm of 1.5 m, a formulation of 9.2 : 90.8 by weight of Azo-6 : RM82 was used, with 2.5 wt% of photoinitiator with respect to the total monomer weight. In a typical sample preparation, 4.6 mg Azo-6, 45.4 mg RM82, and 1.25 mg Irgacure 819 were melted together in a vial and vortexed repeatedly to ensure mixing. The molten monomer mixture was then infiltrated via capillary action into alignment cells on a hot plate at 100°C. The alignment cells were prepared by spin-coating

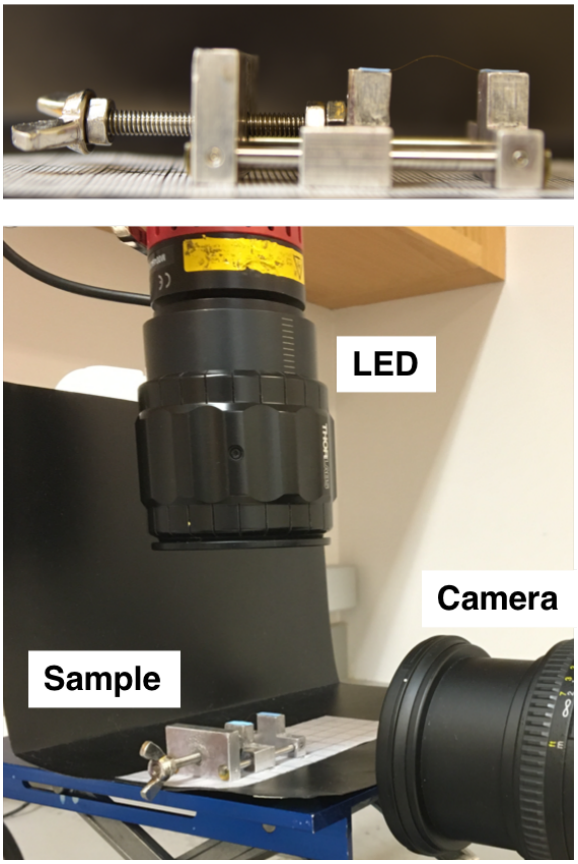

Figure S1: (Top) The sample is fixed at the ends in a home-made compression device. (Bottom) Experimental set-up is composed of a beam illuminated overhead by a UV LED and imaged from the side by a camera.

Elvamide onto clean glass slides, rubbing the slides with a velvet cloth, and gluing the two Elvamide sides facing each other with epoxy mixed with 15 m glass beads. The filled cells were subsequently cooled to 80°C, held isothermal for 5 minutes to induce alignment of the liquid crystalline mesogens, and photopolymerized for 30 minutes with 405 nm light. Following photopolymerization, samples were post-cured at 120°C for 10 minutes and the 15m thick LCNs were harvested by cracking open the alignment cells with a razor blade. Finally, beams of 1 mm in width were cut from the film with the nematic director along the long axis of the strip.

Photoactuation Experiments Buckled beams with dimensions 1 mm x 15 mm x 50 m were prepared by clamping the ends of the film in a home-made film clamp device and compressed to an end-to-end distance of Lfinal/Linitial = 0.95. The buckled film was subsequently illuminated from above with a 365 nm LED (ThorLabs) equipped with a Guassian profile focused onto the sample via an adjustable focusing lens. Each experiment is recorded using a camera (Nikon 5500) fitted with a macrolens operating at a recording speed of 60 frames per second.